Research Square

Preprints are preliminary reports that have not undergone peer review.
They should not be considered conclusive, used to inform clinical practice,
or referenced by the media as validated information.

A Lymphotropic Biomimetic Nanoplatform Reverses Sleep Deprivation-Induced Cognitive Deficits by Reprogramming Microglial Phenotypes

Jun Zhang
Tangdu Hospital, The Fourth Military Medical University
Hongyan Zhou
Tangdu Hospital, The Fourth Military Medical University
Fang Sun
Tangdu Hospital, The Fourth Military Medical University
Ping Yang
School of Basic Medical Sciences, Xi'an Jiaotong University
Kailu Li
Tangdu Hospital, The Fourth Military Medical University
Chunxiang Guan
Tangdu Hospital, The Fourth Military Medical University
Jiaxiu He
Tangdu Hospital, The Fourth Military Medical University
Zhao Zhong
Tangdu Hospital, The Fourth Military Medical University
Shihui Sun
Tangdu Hospital, The Fourth Military Medical University
Qi Wu
Tangdu Hospital, The Fourth Military Medical University
jinyuan Meng
Tangdu Hospital, The Fourth Military Medical University
Hua Xu
Tangdu Hospital, The Fourth Military Medical University
Shaochun Guo
Tangdu Hospital, The Fourth Military Medical University
Peigang Ji
Tangdu Hospital, The Fourth Military Medical University
Kehinde Alare
Ladoke Akintola University of Technology
Gang Zhu

Tangdu Hospital, The Fourth Military Medical University

Changjun Su

Xi'an People's Hospital

Fan Chen

professorchen@foxmail.com

Tangdu Hospital, The Fourth Military Medical University

Research Article

Keywords:

Posted Date: May 27th, 2026

DOI: https://doi.org/10.21203/rs.3.rs-9719018/v1

License: This work is licensed under a Creative Commons Attribution 4.0 International License. Read Full License

Additional Declarations: No competing interests reported.

Version of Record: A version of this preprint was published at Cell Communication and Signaling on October 10th, 2026. See the published version at https://doi.org/10.1186/s12964-026-03291-3.

Abstract

Sleep deprivation (SD) drives persistent neuroinflammation and cognitive impairment, yet the underlying cellular and molecular mechanisms remain incompletely understood. Using single-cell transcriptomics of SD mouse brains, we identify an irreversible microglial phenotype shift characterized by downregulation of the homeostatic marker Tmem119 and upregulation of the disease-associated gene *APOE*. To therapeutically reverse this pathology, we engineered a biomimetic nanoplatform (ATABP) that co-delivers Tmem119-encoding plasmid DNA and an APOE inhibitor. The platform is cloaked with activated microglial membrane for inflammation-directed homologous targeting, and functionalized with ApoA1-mimetic peptides to enable lymphatic trafficking for brain delivery. In SD mice, ATABP treatment restored the homeostatic microglial phenotype, attenuated neuroinflammation, reduced amyloid-β pathology, and rescued cognitive performance without systemic toxicity. This study establishes Tmem119/APOE imbalance as a critical driver of SD-induced neuropathology and demonstrates that lymph-targeted biomimetic nanodelivery offers a promising strategy for microglial reprogramming in SD and potentially other neurological conditions.

Introduction

Sleep deprivation (SD) has emerged as a pervasive public health crisis, with sleep loss associated with cognitive decline and increased susceptibility to neurodegenerative diseases such as Alzheimer's disease (AD) [1–3]. Despite growing recognition of sleep as a fundamental pillar of brain health, the cellular and molecular mechanisms linking sleep disruption to neuronal dysfunction remain incompletely understood, and effective therapeutic interventions for sleep-related cognitive impairment are currently lacking.

Neuroinflammation is increasingly recognized as a central mediator of SD-induced brain pathology, studies have shown that SD elevates pro-inflammatory cytokines—including IL-1β, TNF-α, and IL-6—in both peripheral circulation and brain parenchyma[4, 5]. Microglia, the resident immune cells of the CNS, serve as key effectors in this response, under physiological conditions, microglia maintain a homeostatic surveillance state and providing trophic support to neurons[6, 7]. Upon SD, they undergo marked phenotypic transformations toward activated, pro-inflammatory states[8, 9]. Recent single-cell transcriptomic studies have revealed distinct subpopulations—homeostatic microglia (HOM), disease-associated microglia (DAM), and inflammatory microglia (IFM)—each with unique transcriptional signatures[10, 11]. However, the precise molecular determinants governing microglial phenotypic transitions during SD remain to be fully elucidated.

Among the molecular signatures distinguishing microglial states, TMEM119 and APOE have emerged as particularly informative markers with functional implications. TMEM119, a transmembrane protein selectively expressed in CNS microglia, is a definitive marker of homeostatic identity[12–14]. Critically, a recent study demonstrated that TMEM119 directly binds to Aβ oligomers and promotes their clearance, whereas TMEM119 deficiency accelerates microglial transition from a homeostatic to a disease-

associated state[15]. Conversely, APOE—a stronger genetic risk factor for late-onset AD—is highly expressed in DAM and regulates lipid metabolism and neuroinflammation, exacerbates microglial-mediated neurotoxicity and impairs amyloid-β (Aβ) clearance[16–19]. Notably, TMEM119 and APOE exhibit a reciprocal expression pattern: as microglia transition from homeostatic to disease-associated states, TMEM119 is downregulated while APOE is upregulated[20, 21]. This inverse relationship suggests that the TMEM119/APOE balance may serve as a molecular rheostat for microglial phenotype, yet whether this imbalance represents a causal driver of SD-induced pathology—and whether it can be therapeutically targeted—has not been investigated.

Developing effective therapies for SD-induced cognitive impairment faces significant challenges. Traditional anti-inflammatory agents suffer from poor blood-brain barrier (BBB) penetration, lack of cell-type specificity, and off-target toxicity[22, 23]. Nanomedicine offers promising solutions, engineered nanoparticles can be designed to encapsulate diverse therapeutic cargoes—including nucleic acids, small molecules, and proteins—while providing protection from degradation and enabling controlled release[24, 25]. Surface functionalization with targeting ligands or biomimetic coatings can enhance BBB penetration and confer cell-type specificity[26]. An emerging paradigm for CNS delivery exploits the meningeal lymphatic system as an alternative route to bypass the BBB[27–29]. Recent proof-of-concept studies have demonstrated that nanoparticles engineered with lymphatic homing ligands, such as ApoA1-mimetic peptides, can effectively exploit this pathway to achieve brain delivery[27, 30]. However, the application of targeted nanotherapeutics for microglial reprogramming in sleep disorders remains largely unexplored.

In this study, we hypothesized that SD induces a pathological shift in microglial phenotypes characterized by TMEM119 downregulation and APOE upregulation, and that therapeutic restoration of this balance can reverse cognitive deficits. To test this, we first performed comprehensive single-cell transcriptomic analysis of cortical and hippocampal tissues from SD mouse brains to characterize microglial state transitions. Building on these insights, we engineered a biomimetic nanoplatform (ATABP) co-delivering Tmem119-encoding plasmid DNA and the APOE inhibitor probucol (Fig. 1). The platform features a lymphotropic design comprising activated microglial membrane coating for homologous targeting and ApoA1-mimetic peptides for lymphatic trafficking. We demonstrate that ATABP effectively targets IFM, restores homeostatic gene expression, and rescues cognitive function in SD mice, establishing a proof-of-concept for precision microglial reprogramming via lymph-hitchhiking nanotherapeutics.

Matarials and methods

1. Animals and Sleep Deprivation Model

Adult male C57BL/6J mice (8–10 weeks old, 22–25 g) were obtained from the Laboratory Animal Center of the Fourth Military Medical University (Xi'an, China). All animals were maintained under standard

conditions with a 12-hour light/dark cycle at 22–24°C with free access to food and water. All experimental procedures were performed in accordance with the National Institutes of Health Guide for the Care and Use of Laboratory Animals and approved by the Institutional Animal Care and Use Committee of the Fourth Military Medical University.

SD was performed as previously described. Briefly, mice were subjected to 72 hours of acute sleep deprivation using the multiple platform method. Animals were placed on circular platforms (diameter: 2.5 cm) surrounded by water in a standard home cage. When mice entered sleep (muscle atonia), they would fall into the water and awaken, thereby achieving sleep deprivation. Control mice were placed on larger platforms (diameter: 7 cm) in separate cages under identical conditions, allowing them to sleep without falling into water. For recovery experiments, SD mice were returned to standard housing conditions for 24 or 72 hours before sacrifice.

2. Single-Cell RNA Sequencing Data Analysis

Publicly available single-cell RNA sequencing datasets (GEO accession: GSE137665) derived from cortical and hippocampal tissues of mice under normal sleep, acute sleep deprivation, and recovery sleep conditions were re-analyzed. Data processing was performed using the Seurat package (version 5.3.0) in R. Cells with < 200 genes and > 20% mitochondrial reads were excluded. Principal component analysis was performed on the most variable genes, and cells were clustered using the Louvain algorithm at a resolution of 0.4. Cell types were annotated based on canonical marker genes: microglia (P2ry12, Tmem119, Cx3cr1), neurons (Rbfox3/NeuN, Snap25), astrocytes (Gfap, Aqp4), and oligodendrocytes (Olig2, Mbp). For microglial subclustering, cells were re-clustered at higher resolution (0.6), revealing three distinct subpopulations: HAM, DAM, and inflammatory microglia. Pseudotime trajectory analysis was performed using Monocle 2. Gene ontology enrichment analysis was conducted using clusterProfiler with the Benjamini-Hochberg correction for multiple comparisons (adjusted $P < 0.05$).

3. Cell Culture

BV2 murine microglial cells (ATCC) were cultured in Dulbecco's Modified Eagle's Medium (DMEM, Gibco) supplemented with 10% fetal bovine serum (FBS, Gibco), 100 U/mL penicillin, and 100 μg/mL streptomycin at 37°C in a 5% CO_2 humidified atmosphere. GL261 glioma cells (ATCC), HA1800 human astrocytes (ScienCell) and bEnd.3 mouse brain endothelial cells (ATCC) were cultured in DMEM/10% FBS. For microglial activation, cells were treated with 100 ng/mL lipopolysaccharide (LPS, Sigma) and 20 ng/mL interferon-γ (IFN-γ, PeproTech) for 24 h.

4. Preparation of Biomimetic Nanoplatform (ATABP)

The ATABP nanoplatform was constructed using a three-step procedure. First, PLGA nanoparticles (NPs) were prepared by a double emulsion solvent evaporation method as previously described. Briefly, 50 mg of PLGA (50:50, MW 30 kDa, Lactel) was dissolved in 1 mL of dichloromethane (DCM). Tmem119-encoding plasmid DNA (cDNA, 100 μg, GenScript) and probucol (APOE inhibitor, Sigma) were emulsified in 200 μL of PBS containing 1% polyvinyl alcohol (PVA, Sigma) using a probe sonicator (Sonics, 30% amplitude, 30 s). This primary emulsion was added to 5 mL of 2% PVA and sonicated again (30% amplitude, 60 s). The resulting double emulsion was stirred overnight at room temperature to evaporate DCM, and NPs were collected by centrifugation (20,000 × g, 20 min, 4°C).

Second, microglial membranes were extracted from IFN-γ/LPS-activated BV2 cells using a membrane protein extraction kit (Thermo Fisher Scientific) according to the manufacturer‘s protocol. The membrane suspension was extruded through a 200-nm polycarbonate membrane 10 times using a mini-extruder to form membrane vesicles. PLGA NPs were mixed with membrane vesicles at a 1:1 protein-to-polymer weight ratio and co-extruded through 100-nm membranes 11 times to produce membrane-coated NPs (M-NPs).

Third, ApoA1-mimetic peptide was conjugated to the surface of M-NPs via maleimide-thiol chemistry. The peptide (0.5 mg/mL) was incubated with M-NPs (1 mg/mL) in PBS (pH 7.4) for 4 h at room temperature with gentle shaking. Unconjugated peptide was removed by centrifugation (20,000 × g, 20 min). The final product, designated ATABP, was stored at 4°C in PBS.

5. Nanoparticle Characterization

The morphology of nanoparticles was visualized using transmission electron microscopy (TEM). Samples were negatively stained with 2% uranyl acetate and imaged at an accelerating voltage of 120 kV. Hydrodynamic diameter, polydispersity index (PDI), and zeta potential were measured by dynamic light scattering (DLS) using a Zetasizer Nano ZS (Malvern Instruments). Each measurement was performed in triplicate at 25°C. Encapsulation efficiency of cDNA was determined using a Quant-iT RiboGreen assay (Thermo Fisher Scientific) following the manufacturer‘s instructions. Encapsulation efficiency of probucol was determined by high-performance liquid chromatography (HPLC, Agilent 1260 Infinity). For stability assessment, nanoparticles were stored in **PBS or DMEM** containing 10% FBS at 4°C for 7 days, and size and PDI were measured daily.

6. Western Blot Analysis of Membrane Protein Retention

6. Western Blot Analysis of Membrane Protein Retention
To confirm successful membrane coating, nanoparticle samples (20 μg protein equivalent) were lysed in RIPA buffer (50 mM Tris-HCl pH 7.4, 150 mM NaCl, 1% NP-40, 0.5% sodium deoxycholate, 0.1% SDS) supplemented with protease inhibitor cocktail (Roche). Proteins were separated by 10% SDS-PAGE and transferred to PVDF membranes (Millipore). Membranes were blocked with 5% non-fat milk in TBST for 1

h at room temperature and incubated overnight at 4°C with primary antibodies against CX3CR1 (1:500, Abcam), Iba1 (1:1000, Wako), and β-actin (1:5000, Cell Signaling Technology). After washing, membranes were incubated with HRP-conjugated secondary antibodies (1:5000, Cell Signaling) for 1 h at room temperature. Protein bands were visualized using enhanced chemiluminescence (Thermo Fisher Scientific) and quantified using ImageJ software. Coomassie Brilliant Blue staining was performed on SDS-PAGE gels to visualize total protein profiles of membrane lysates and nanoparticle samples.

7. In Vitro Cellular Uptake and Targeting Specificity

For uptake studies, nanoparticles were labeled with the near-infrared dye Ce6 (Sigma) during preparation. BV2 microglia (activated or resting), GL261 glioma cells, or primary mouse astrocytes were seeded in confocal microscopy dishes (1×10^5 cells/well) and incubated with Ce6-labeled nanoparticles (50 μg/mL) for 4 h at 37°C. The efficiency of microglia uptake of the nanoparticles was determined using confocal laser scanning microscopy. Image quantification was performed using ImageJ.

8. In Vitro Gene Delivery and Functional Assays

Activated BV2 cells were treated with ATABP or control nanoparticles (50 μg/mL) for 48 h. Tmem119 mRNA levels were quantified by qRT-PCR using TaqMan probes (Thermo Fisher). For Western blot, cell lysates (30 μg) were probed with anti-TMEM119 (1:500, Abcam). Cytokine levels (IL-1β、IL-6、IL-10、TNF-α) in culture supernatants were measured by ELISA (R&D Systems).

9. Posterior Cervical Injection and In Vivo Imaging

Mice received a single subcutaneous injection of Ce6-labeled nanoparticles (5 mg/kg in 50 μL PBS). Whole-body fluorescence imaging was performed at 4, 8, and 24 h post-injection using an IVIS Spectrum system (ex/em: 620/670 nm). Fluorescence intensity was quantified in lymph nodes, brain, and major organs. At endpoint, tissues were collected for ex vivo imaging.

10. Immunofluorescence and Immunohistochemistry

Perfused brains were post-fixed in 4% PFA, cryoprotected in 30% sucrose, and frozen in OCT. Coronal sections were blocked with 5% donkey serum/0.3% Triton X-100 and incubated overnight at 4°C with primary antibodies against Iba1, TMEM119, Aβ. After washing, sections were incubated with Alexa Fluor-conjugated secondary antibodies and counterstained with DAPI. Images were acquired on a confocal or fluorescence microscope.

11. Behavioral Testing

Y-maze: Mice were placed in a Y-shaped maze (arms: 35 cm) and allowed to explore for 8 min. Spontaneous alternation (%) was calculated as: (alternations / (total arm entries − 2)) × 100%. Novel object recognition: After a 10 min training session with two identical objects, mice were tested 24 h later with one object replaced by a novel object. Recognition index = time with novel / total exploration time × 100%; Discrimination index = (time with novel − time with familiar) / total exploration time × 100%.

12. Hematoxylin and Eosin Staining and Safety Assessment

Major organs (heart, liver, spleen, lungs, kidneys, brain) were fixed, paraffin-embedded, sectioned (5 μm), and stained with H&E. Slides were examined by a blinded pathologist for histopathological changes. Serum ALT, AST, T-BIL, D-BIL, ALB, ALP, GGT, TBA, CREA, UA and BUN were measured using a clinical chemistry analyzer. Body weight was monitored daily for 30 days.

13. Hemolysis Assay

Mouse red blood cells (2% v/v in PBS) were incubated with ATABP at 37°C for 1 h. After centrifugation, supernatant absorbance at 540 nm was measured. Hemolysis (%) was calculated relative to water (100%) and PBS (0%).

14. **Statistical Analysis**

Data are presented as mean ± SEM. Comparisons between two groups were made using unpaired two-tailed Student‘s t-test. Multiple comparisons were analyzed by one-way or two-way ANOVA with Tukey’s or Sidak‘s post hoc test. Correlations were assessed using Pearson’s correlation coefficient. Significance was set at *P < 0.05, **P < 0.01, ***P < 0.001. All experiments were performed with at least three biological replicates.

Results

1. Single-Cell Transcriptomic Analysis Identifies an Irreversible Tmem119/APOE Imbalance as a Driver of Sleep Deprivation-Induced Microglial Pathology

To dissect the cellular and molecular mechanisms underlying SD-induced neuroinflammation, we re-analyzed a publicly available single-cell RNA sequencing dataset (GEO: GSE137665) derived from cortical and hippocampal tissues of mice under normal sleep (NS), acute SD, and recovery sleep (RS) conditions. Unbiased clustering of all cells revealed major CNS cell types, including neurons, astrocytes, oligodendrocytes, and microglia et al, in both the hippocampus and cortex (Fig. 2A-D). Among all CNS cell types, microglia exhibited the most pronounced transcriptional response to SD[31, 32]. Differential gene expression analysis across cell types revealed that microglia harbored the largest number of SD-induced changes, particularly in pathways related to inflammation, phagocytosis, and metabolic stress[31, 33, 34]. Given their central position as primary immune sentinels and their emerging involvement in sleep-wake

regulation, we focused subsequent analyses on the heterogeneity and dynamic remodeling of microglial subpopulations.

Focusing on microglia, subclustering resolved three transcriptionally distinct subpopulations: HOM characterized by P2ry12 and Tmem119; DAM defined by Apoe and Trem2; and IFM marked by Il1b and Cd83 (Fig. 2E-H). Quantification of subset proportions revealed a striking and regionally distinct pathological remodeling. In the hippocampus, SD induced a profound ~ 65% reduction in HOM, which failed to return to baseline levels even after RS (Fig. 2I). IFM expanded dramatically by approximately 3-fold during SD and also did not recover to near-baseline levels after RS, whereas DAM showed an increase during SD followed by a modest sustained accumulation during the recovery period (Fig. 2I). In the cortex, microglial subset dynamics exhibited a similar pattern: HOM was significantly reduced after SD and recovered to near-baseline levels following RS. SD induced IFM expanded acutely, while normalized after RS, and DAM also showed a modest increase during SD (Fig. 2J). These data indicate that both the hippocampus and cortex are vulnerable to SD-induced loss of microglial homeostatic identity, which fails to fully restore even after RS. We next performed pseudotime ordering of all microglial cells to infer state transition dynamics. The trajectory revealed a continuous, unidirectional progression from HOM through DAM to IFM (Fig. 2K, S1A–B). Along this pseudotime axis, HOM signature genes, including Cx3cr1, P2ry12 notably Tmem119 and Inpp5d, progressively declined, with the most pronounced downregulation observed in IFM (Fig. 2L). In contrast, DAM-associated genes, particularly Apoe and Lyz2, steadily increased along the trajectory and remained elevated in IFM (Fig. 2M). The hallmark genes of IFM are only expressed in IFM (Fig. 1C). To further identify candidate genes, we performed qPCR on cortical and hippocampal tissues from independent cohorts of NS and SD mice. Consistent with the single-cell data, SD induced a significant reduction in Tmem119 expression in both brain regions (Fig. 2N-O) and a marked increase in Apoe expression (Fig. 2P-Q). Changes in other signature genes, including Inpp5d and Lyz2, were less robust (S1D-G). Based on the magnitude of expression change, their central position in the pseudotime trajectory, and their established functional roles in microglial homeostasis and disease-associated states, we selected Tmem119 and Apoe as the most promising therapeutic targets for reversing SD-induced microglial pathology (Fig. 2R).

2. Engineering and Characterization of the Biomimetic Nanoplatform (ATABP)

To achieve targeted microglial reprogramming, we engineered a biomimetic nanoplatform (termed ATABP) with a hierarchical architecture. The core consists of PLGA co-encapsulating Tmem119 plasmid DNA (cDNA) and the APOE inhibitor probucol (PU). This core is cloaked with an activated microglial membrane (derived from IFN-γ/LPS-stimulated BV2 cells) and further functionalized with ApoA1-mimetic peptides to confer lymphatic homing (Fig. 3A). Given the inherent instability and negative charge of cDNA, we first complexed it with cationic chitosan (CS) to enhance encapsulation. Gel retardation assays showed that free pDNA migrated freely, whereas the CS-pDNA complex and the PLGA-loaded complex remained trapped in the wells, confirming successful pDNA encapsulation (Fig. 3B-C). Systematic screening of PLGA:PU ratios identified a 5:1 ratio as optimal, yielding the highest

encapsulation efficiency (EE) and loading efficiency (LE) while maintaining favorable particle size (Fig. 3D-E).

Transmission electron microscopy (TEM) revealed that both AB@PLGA (membrane-coated without cDNA and PU) and the fully assembled ATABP displayed a distinct core-shell morphology with a visible ring-like membrane structure, which was absent in bare PLGA nanoparticles (Fig. 3F, S2A). Dynamic light scattering (DLS) confirmed a uniform hydrodynamic diameter of 198 ± 6.5 nm and a zeta potential of − 22.3 ± 1.5 mV for ATABP (Fig. 3G-H). Importantly, ATABP maintained colloidal stability in both PBS and DMEM over 7 days of storage at − 20°C, with no significant size aggregation (Fig. 3I, S2B). Western blot analysis confirmed the successful retention of key microglial surface proteins—including CX3CR1, Iba1, and CD11b—on the ATABP coating, indicating that the membrane cloaking process preserved immunologically relevant surface markers (Fig. 3J, S2C). Coomassie Blue staining further demonstrated that the majority of the membrane protein profile was retained on the nanoparticles (Fig. 3K, S2C), a finding corroborated by BCA protein quantification (Fig. S2D). Finally, to evaluate whether the engineered platform could deliver its therapeutic cargo, we incubated ATABP with BV2 microglia and assessed Tmem119 expression. qPCR analysis revealed a significant upregulation of Tmem119 mRNA in ATABP-treated cells compared to controls, confirming that the nanoplatform successfully delivers functional cDNA and drives target gene expression in microglia (Fig. 3L).

3. ATABP specifically targets inflammatory microglia and exerts therapeutic reprogramming in vitro

To evaluate the targeting specificity of the biomimetic platform, we incubated Ce6-labeled nanoparticles —PLGA, AB-PLGA (membrane-coated without cargo), and fully assembled ATABP—with IFN-γ/LPS-activated BV2 cells, resting BV2 cells, GL261 glioma cells, and primary mouse astrocytes. Confocal imaging revealed that both AB-PLGA and ATABP were efficiently internalized by activated BV2 cells, with ATABP exhibiting approximately 6-fold higher uptake than bare PLGA (Fig. 4A–B). Among all cell types tested, IFN-γ/LPS-activated BV2 cells showed the highest phagocytic capacity for AB-PLGA and ATABP, demonstrating that the activated state enhances recognition of the homologous membrane coating. This finding is consistent with previous reports that microglial membrane-coated nanoparticles preferentially accumulate in inflamed brain regions via homotypic adhesion interactions, such as VCAM-1/integrin α4/β1[35].

We next examined whether modulating microglial phenotype alters ATABP uptake. ATABP was incubated with resting BV2 cells, IFN-γ/LPS-activated BV2 cells, and activated BV2 cells that were either Tmem119-overexpressing, treated with PU, or both. Activated BV2 cells exhibited the highest uptake efficiency, whereas Tmem119 overexpression or PU treatment significantly reduced internalization (Fig. 4C–D). These data suggest that the inflammatory state—rather than a single surface marker—governs homologous recognition, and that therapeutic restoration of homeostatic features (Tmem119 upregulation) or suppression of disease-associated pathways (APOE inhibition) diminishes this

targeting. Western blot analysis showed that both ATBP (lacking PU) and ATABP (full formulation) significantly upregulated Tmem119 protein expression in activated BV2 cells, confirming successful gene delivery (Fig. 4E). Importantly, this phenotypic shift was accompanied by a profound modulation of cytokine secretion. ELISA measurements revealed that ATABP treatment significantly reduced the levels of pro-inflammatory cytokines IL-1β, TNF-α, and IL-6, while concurrently elevating the anti-inflammatory cytokine IL-10 in the culture supernatant (Fig. 4F-I). These results demonstrate that ATABP not only delivers its genetic cargo but also functionally reprograms inflammatory microglia toward a homeostatic, anti-inflammatory phenotype.

Finally, we assessed whether ATABP-mediated reprogramming improved the functional capacity of inflammatory microglia. Activated BV2 cells treated with ATABP were incubated with fluorescently labeled lipid microspheres as Aβ-mimetic phagocytic targets. Confocal imaging and quantitative analysis showed that ATABP-treated cells exhibited a significantly higher uptake of these particles compared to untreated activated controls (Fig. 4J-K). This enhanced phagocytic activity indicates that restoring Tmem119 expression and suppressing APOE function synergistically improves microglial clearance capability, a critical effector function for mitigating neuroinflammation and protein aggregation.

4. ATABP achieves targeted brain delivery via a lymphotropic trafficking pathway in vivo.

To evaluate the in vivo trafficking of ATABP, we subcutaneously administered Ce6-labeled nanoparticles —PLGA, TABP (no ApoA1), AABP (no Tmem119 cDNA), ATBP (no PU), and fully assembled ATABP—to SD mice at the posterior cervical midline. Ex vivo imaging of lymph nodes harvested 4 hours post-injection revealed that AABP, ATBP, and ATABP all exhibited strong fluorescence accumulation in both deep cervical lymph nodes (dCLNs) and superficial cervical lymph nodes (spCLNs), whereas axillary (aLN) and inguinal (inLN) lymph nodes showed minimal signal (Fig. 5A-C, S3A-B). In contrast, intravenous administration of ATABP resulted in weak but detectable distribution across all lymph node groups, while subcutaneous injection in wild-type mice produced a similar pattern to that observed in SD mice (Fig. 5A-C). Notably, TABP (lacking ApoA1) showed markedly reduced cervical lymph node accumulation, demonstrating that the ApoA1-mimetic peptide is essential for lymph node homing.

We next performed longitudinal in vivo imaging to track nanoparticle delivery to the brain. In mice receiving AABP, ATBP, or ATABP, fluorescence signal in the brain became detectable at 4 hours post-injection, peaked at 8 hours, and gradually declined by 24 hours (Fig. 5D-F, S3C-D). ATABP administered intravenously produced only minimal brain accumulation at 24 hours, while subcutaneous injection in wild-type mice yielded an intermediate signal (Fig. 5D-F). Ex vivo quantification of brain fluorescence at 8 hours confirmed that AABP, ATBP, and ATABP groups exhibited significantly higher brain accumulation compared to the intravenous or TABP groups (Fig. 5G–H). This time-dependent brain trafficking from cervical lymph nodes is consistent with the established anatomy of the glymphatic-lymphatic system,

wherein nanoparticles can travel retrogradely from cervical lymph nodes to the brain via meningeal lymphatic vessels. Immunofluorescence analysis of cervical lymph node sections confirmed that AABP, ATBP, and ATABP were abundantly distributed within dCLNs and spCLNs, whereas intravenous administration resulted in only sparse nodal accumulation (Fig. 5I, S4A-C). In the brain, confocal imaging of cortical and hippocampal sections revealed that AABP, ATBP, and ATABP all exhibited substantial parenchymal accumulation, with ATABP showing the most pronounced colocalization with Iba1 + microglia (Fig. 5J, S5A-C). This microglial-specific targeting is consistent with the homologous recognition conferred by the microglial membrane coating, a principle that has been validated in multiple CNS disease models[36, 37].

Finally, we assessed the biodistribution of ATABP in major peripheral organs. Ex vivo imaging of heart, liver, spleen, lungs, and kidneys revealed that subcutaneous administration of ATABP, AABP, ATBP, or TABP resulted in minimal fluorescence accumulation in any of these organs (Fig. S6). In striking contrast, intravenous administration of ATABP led to substantial accumulation in the liver. These data demonstrate that the lymphotropic subcutaneous route effectively bypasses hepatic sequestration, achieving brain-targeted delivery with reduced off-target toxicity.

5. ATABP rescues cognitive deficits and restores microglial homeostasis in sleep-deprived mice

To evaluate the therapeutic efficacy of ATABP, we subjected mice to 72 hours of SD followed by subcutaneous administration of various formulations. Cognitive function was assessed using the Y-maze and novel object recognition (NOR) tests. SD mice exhibited a marked reduction in spontaneous alternation in the Y-maze and discrimination index in the NOR test compared to normal controls, indicating profound working memory and recognition memory deficits (Fig. 6A-H). Treatment with the complete ATABP formulation fully restored both behavioral measures to levels nearly to healthy controls. In contrast, mice receiving partial formulations—PLGA (empty carrier), AABP (lacking Tmem119 pDNA), or ATBP (lacking APOE inhibitor)—showed only partial or no improvement, demonstrating that both Tmem119 restoration and APOE inhibition are required for full cognitive recovery (Fig. 6A-H). A schematic summary of the proposed therapeutic mechanism is presented in Fig. 6I.

To further explore the mechanism of ATABP treatment, we investigated the proportion of TMEM119 + homeostatic microglia and Aβ clearance rate in mouse brain tissue after treatment. Immunofluorescence analysis of brain sections revealed that SD induced a substantial reduction in TMEM119 + microglia in both the cortex and hippocampus, accompanied by accumulation of Aβ plaques (Fig. 7A-B, S7A-F). Treatment with ATABP significantly increased the density of TMEM119 + cells and reduced Aβ plaque burden in both brain regions, whereas AABP or ATBP produced only modest effects (Fig. 7A-B, S7A-F). Immunohistochemical quantification of Iba1 + TMEM119+ double-positive microglia further confirmed that ATABP and ATBP treatments yielded the highest proportions of homeostatic microglia (Fig. 7C-H). These data demonstrate that ATABP effectively restores the

homeostatic microglial signature and enhances amyloid-β clearance. This is consistent with the established role of TMEM119 in promoting Aβ phagocytosis, as recent studies have shown that TMEM119 directly binds Aβ oligomers and facilitates their lysosomal degradation[38]. High-resolution confocal imaging of Iba1-stained microglia revealed that SD induced a characteristic amoeboid morphology with reduced branch complexity and enlarged soma area—hallmarks of inflammatory activation (Fig. 7I). Sholl analysis confirmed that microglia in SD mice exhibited significantly fewer branch intersections and increased soma size compared to controls (Fig. 7J–L). ATABP treatment strikingly reversed this pathological morphology, restoring a ramified, highly branched architecture with reduced soma area, indicative of a return to homeostatic surveillance function (Fig. 7I–L). Western blot analysis of cortical and hippocampal lysates confirmed that ATBP and ATABP treatments significantly increased Tmem119 protein expression compared to SD or empty-vector controls (Fig. 7M, S8). Moreover, ELISA measurements of brain homogenates revealed that AABP, ATBP, and ATABP all reduced the levels of pro-inflammatory cytokines IL-1β and TNF-α, with ATABP achieving the greatest suppression—reducing levels to near those of healthy control mice (Fig. 7N-O). These data collectively demonstrate that ATABP exerts its therapeutic effects by simultaneously restoring homeostatic microglial gene expression and suppressing the inflammatory secretome, thereby creating a brain microenvironment conducive to synaptic health and cognitive function.

Discussion

The present study provides the first comprehensive single-cell transcriptomic characterization of microglial phenotypic dynamics in SD mouse brains, revealing an irreversible loss of HOM identity that persists despite recovery sleep, and identifies the Tmem119/Apoe molecular axis as a key driver of this pathology. Our finding that HOM are depleted by approximately 65% following SD, with no rescue even after RS, fundamentally challenges the prevailing assumption that sleep restoration is sufficient to reverse SD-induced brain pathology. While prior studies have documented SD-induced cytokine elevation and microglial activation[39–41], the persistence of microglial state transitions beyond the acute deprivation period has not been previously demonstrated at single-cell resolution. Notably, the concurrent expansion of IFM by approximately 3-fold during SD, which also failed to fully normalize after RS, suggests that both hippocampal and cortical microglial homeostasis are profoundly disrupted. Pseudotemporal trajectory analysis revealed a unidirectional continuum from HAM through DAM to IFM states, along which Tmem119 progressively declined while Apoe steadily increased. The functional significance of TMEM119 downregulation is underscored by recent evidence that TMEM119 directly binds Aβ to facilitate its clearance, and that its deficiency accelerates AD pathology[42]. Conversely, pathological Apoe upregulation in DAM impairs lipid metabolism and suppresses Aβ clearance through TREM2-APOE pathway dysregulation[43–45]. The dual-target strategy of restoring Tmem119 while suppressing Apoe is therefore mechanistically synergistic, explaining the superior efficacy of ATABP over partial constructs in behavioral assays.

The biomimetic design of ATABP, combining activated microglial membrane coating with ApoA1-mimetic peptide functionalization, achieves hierarchical targeting of inflammatory microglia through homologous recognition mechanisms. The enhanced uptake of ATABP by activated BV2 cells compared to resting cells—approximately 6-fold higher than bare PLGA—is consistent with the established principle of cell membrane-coated nanotechnology, wherein the source cell's surface proteome confers targeting specificity to cells of the same lineage[46, 47]. This homotypic targeting effect has been extensively documented across various cell types, including cancer cells, stem cells, and immune cells[48, 49]. Specifically for microglial membrane coatings, previous studies have demonstrated that BV2 membrane-coated formulations exhibit preferential internalization by Aβ1-42-induced BV2 cells, with uptake significantly hindered by anti-VCAM-1 antibody, identifying the VCAM-1/integrin α4/β1 interaction as a key mediator of this targeting mechanism[27]. The inflammatory state of target microglia appears to facilitate this recognition, as activated microglia upregulate surface adhesion molecules that interact with complementary proteins retained on the homologous membrane coating[47]. This inflammation-dependent targeting is further supported by findings that microglia-derived membranes enhance nanoparticle uptake by both glioma cells and tumor-associated microglia in glioblastoma models[50]. Importantly, the microglial membrane coating also reduces nonspecific activation of recipient microglia, a desirable property for neuroinflammatory applications[46]. The additional ApoA1-mimetic peptide functionalization enables the nanocarrier to exploit the cervical lymphatic drainage pathway for brain delivery—a paradigm shift that circumvents the restrictive BBB. Following subcutaneous injection, ATABP accumulated preferentially in cervical lymph nodes, with subsequent brain trafficking correlating positively with lymph node accumulation. This lymph-to-brain route is consistent with the established glymphatic-lymphatic anatomy, wherein meningeal lymphatic vessels drain CSF and interstitial fluid into deep cervical lymph nodes[51, 52]. Notably, recent work has directly demonstrated retrograde nanoparticle trafficking from cervical lymph nodes to the brain via this network[50]. Critically, this lymphotropic approach achieved brain delivery with minimal peripheral organ accumulation, avoiding reticuloendothelial system clearance and reducing off-target toxicity.

The therapeutic efficacy of ATABP in rescuing cognitive function in SD mice is mechanistically grounded in the restoration of microglial homeostasis. The positive correlation between Y-maze performance and TMEM119 + microglial density across individual animals provides compelling evidence that cognitive recovery is causally linked to microglial reprogramming. This link is further supported by Sholl analysis demonstrating morphological recovery of microglia from amoeboid to ramified states following ATABP treatment. This link is further supported by ELISA data showing that ATABP treatment significantly reduced pro-inflammatory cytokines IL-1β and TNF-α while elevating anti-inflammatory IL-10. The reduction in Aβ plaque burden following ATABP treatment suggests that microglial reprogramming restores phagocytic clearance mechanisms, consistent with evidence linking sleep-dependent glymphatic Aβ clearance to AD risk[53, 54]. Notably, microglia have been shown to be essential for protecting memories formed during SD[55, 56], and our findings extend this concept by demonstrating that

restoring microglial homeostatic function actively reverses, rather than merely preserves, cognitive deficits.

Compared to existing therapeutic approaches, ATABP offers distinct advantages by combining cell-type-specific targeting, dual-cargo co-delivery, and lymphotropic brain access. Current pharmacological interventions—including sedative-hypnotics and anti-inflammatory agents—address symptoms rather than underlying microglial pathology and are associated with significant side effects such as tolerance, dependence, and immunosuppression[57, 58]. Gene therapy approaches face challenges of delivery specificity and immunogenicity[59, 60]. The use of probucol as an APOE inhibitor is clinically relevant: probucol is an FDA-approved lipid-lowering agent with an established safety profile, and its repurposing for neuroinflammatory indications is supported by evidence of its anti-inflammatory and antioxidant properties in the CNS[61, 62]. The combination of a clinically validated small molecule with Tmem119 plasmid within a single nanoplatform exemplifies the potential of combinatorial nanomedicine to achieve synergistic effects that neither agent could accomplish alone. Moreover, the comprehensive safety assessment further supporting its translational potential.

There are several limitations merit consideration. First, while we validated key findings by PCR in our own SD mouse model, the causal relationship between Tmem119/Apoe imbalance and cognitive deficits requires confirmation through genetic loss- and gain-of-function experiments. Second, the therapeutic efficacy of ATABP in chronic sleep restriction models, which more closely approximate clinical sleep disorders, remains to be established. Third, anatomical differences in lymphatic drainage between rodents and humans may necessitate optimization of injection site and nanoparticle formulation for clinical translation. Future studies should also explore the applicability of the ATABP platform to other neuroinflammatory conditions where the Tmem119/Apoe may represent a shared therapeutic target, including AD, Parkinson's disease, and traumatic brain injury.

Conclusion

In this study, we demonstrate that SD triggers an irreversible microglial pathology characterized by persistent loss of HOM and expansion of IFM, with Tmem119 downregulation and Apoe upregulation identified as the core molecular signature through single-cell transcriptomics of mouse cortical and hippocampal tissues. To therapeutically address this pathology, we engineered a lymphotropic biomimetic nanoplatform (ATABP) that co-delivers a Tmem119-encoding plasmid and the APOE inhibitor probucol, cloaked with activated microglial membrane and functionalized with ApoA1-mimetic peptides. Following subcutaneous cervical injection, ATABP exploits the meningeal lymphatic system for efficient brain delivery—achieving significantly higher brain accumulation than intravenous administration while avoiding hepatic sequestration—and selectively targets inflammatory microglia through homologous recognition mediated by the microglial membrane coating. In SD mice, ATABP treatment restores the HOM phenotype, rescues cognitive deficits, reduces neuroinflammation, clears Aβ pathology, and exhibits no systemic toxicity across multiple safety parameters. Collectively, these findings establish the Tmem119/Apoe imbalance as a druggable driver of SD-induced neuropathology and validate lymph-

hitchhiking nanodelivery as a transformative strategy for precision microglial reprogramming in the brain, with potential applicability to other neuroinflammatory disorders sharing this molecular axis.

Declarations

Funding

This research was supported by the Fund of Tang Du hospital (No.2021YFJH005 and N0.2025JCRH030), National Natural Science Foundation of China (No.82201643) and “Phoenix Introduction Plan” Talent Startover Project of Tangdu Hospital, Fourth Military Medical University (No.2021YFJH003).

Author Contribution

J.Z.: Investigation, Formal analysis, Data curation, Methodology, Writing–original draft. H.Y.: Investigation, Formal analysis, Validation, Writing–original draft. F.S.: Investigation, Formal analysis, Writing–original draft. P.Y.: Formal analysis, Data curation. K.L.: Formal analysis, Data curation. C.X.: Formal analysis, Data curation. Z.Z.: Formal analysis, Data curation. Q.W.: Formal analysis. J.Y.: Formal analysis. S.H.: Formal analysis. H.X.: Formal analysis. S.C.:Data curation. P.G.:Data curation. K.A.:Data curation. G.Z.: Writing – review & editing. C.J.: Writing – review & editing. F.C.: Conceptualization, Funding acquisition, Supervision, Writing – original draft, Writing – review & editing.

Data Availability

RNA-seq analysis on mouse brain was sourced from publicly available single-cell RNA sequencing datasets (GEO accession: GSE137665). Experimental data related to these findings are accessible from the corresponding author upon justified request.

References

1. Huang, T., Beydoun, M.A., Kianersi, S., Redline, S. & Launer, L.J. Multi-dimensional sleep health and dementia risk: a prospective study in the UK Biobank. *BMC Med* **23**, 410 (2025).
2. Best, P.T. et al. Association of Changes in Cerebral and Hypothalamic Structure With Sleep Dysfunction in Patients With Genetic Frontotemporal Dementia. *Neurology* **103**, e209829 (2024).
3. Oh, J.Y. et al. Subcortical Neuronal Correlates of Sleep in Neurodegenerative Diseases. *JAMA Neurol* **79**, 498–508 (2022).
4. Irwin, M.R. Sleep and inflammation: partners in sickness and in health. *Nat Rev Immunol* **19**, 702–715 (2019).
5. Cho, C.H., Kim, D.H., Baek, E.H. & Kim, D.H. Serum Levels of TNF-α Are Increased in Patients with Rotator Cuff Tear and Sleep Disturbance. *Diagnostics (Basel)* **11** (2021).

6. Scheiblich, H., Trombly, M., Ramirez, A. & Heneka, M.T. Neuroimmune Connections in Aging and Neurodegenerative Diseases. *Trends Immunol* **41**, 300–312 (2020).
7. Wang, Z. et al. Early life high fructose impairs microglial phagocytosis and neurodevelopment. *Nature* **644**, 759–768 (2025).
8. Parhizkar, S. et al. Sleep deprivation exacerbates microglial reactivity and Aβ deposition in a TREM2-dependent manner in mice. *Sci Transl Med* **15**, eade6285 (2023).
9. Li, X., Kong, Z., Cai, K., Qi, F. & Zhu, S. Neopterin mediates sleep deprivation-induced microglial activation resulting in neuronal damage by affecting YY1/HDAC1/TOP1/IL-6 signaling. *J Adv Res* **72**, 181–195 (2025).
10. Pilat, D.J. et al. The gain-of-function TREM2-T96K mutation increases risk for Alzheimer's disease by impairing microglial function. *Neuron* **114**, 46–66.e13 (2026).
11. Wilson, E.N. et al. TREM1 disrupts myeloid bioenergetics and cognitive function in aging and Alzheimer disease mouse models. *Nat Neurosci* **27**, 873–885 (2024).
12. Fitz, N.F. et al. Trem2 deficiency differentially affects phenotype and transcriptome of human APOE3 and APOE4 mice. *Mol Neurodegener* **15**, 41 (2020).
13. Ennerfelt, H. et al. SYK coordinates neuroprotective microglial responses in neurodegenerative disease. *Cell* **185**, 4135–4152.e4122 (2022).
14. Atkinson, J.R. et al. Biological aging of CNS-resident cells alters the clinical course and immunopathology of autoimmune demyelinating disease. *JCI Insight* **7** (2022).
15. Liu, J. et al. Microglial TMEM119 binds to amyloid-β to promote its clearance in an Aβ-depositing mouse model of Alzheimer's disease. *Immunity* **58**, 1830–1846.e1837 (2025).
16. Ulrich, J.D. et al. ApoE facilitates the microglial response to amyloid plaque pathology. *J Exp Med* **215**, 1047–1058 (2018).
17. Krasemann, S. et al. The TREM2-APOE Pathway Drives the Transcriptional Phenotype of Dysfunctional Microglia in Neurodegenerative Diseases. *Immunity* **47**, 566–581.e569 (2017).
18. Fortea, J. et al. APOE4 homozygozity represents a distinct genetic form of Alzheimer's disease. *Nat Med* **30**, 1284–1291 (2024).
19. Kaji, S. et al. Apolipoprotein E aggregation in microglia initiates Alzheimer's disease pathology by seeding β-amyloidosis. *Immunity* **57**, 2651–2668.e2612 (2024).
20. Cao, Z. et al. Unique Subtype of Microglia in Degenerative Thalamus After Cortical Stroke. *Stroke* **52**, 687–698 (2021).
21. Zhou, Y. et al. Human and mouse single-nucleus transcriptomics reveal TREM2-dependent and TREM2-independent cellular responses in Alzheimer's disease. *Nat Med* **26**, 131–142 (2020).
22. Zhang, X. et al. Blood-brain barrier penetrating carbon dots with intrinsic anti-inflammatory and drug-loading properties. *Biomater Adv* **139**, 212995 (2022).
23. Zhao, Y. et al. Neutrophil Membrane-Camouflaged Polyprodrug Nanomedicine for Inflammation Suppression in Ischemic Stroke Therapy. *Adv Mater* **36**, e2311803 (2024).

24. Mitchell, M.J. et al. Engineering precision nanoparticles for drug delivery. *Nat Rev Drug Discov* **20**, 101–124 (2021).
25. Dai, X.J. et al. Stimuli-Responsive Nano Drug Delivery Systems for the Treatment of Neurological Diseases. *Small* **21**, e2410030 (2025).
26. Liao, J. et al. Revolutionizing Neurocare: Biomimetic Nanodelivery Via Cell Membranes. *Adv Mater* **36**, e2402445 (2024).
27. Wang, H.C. et al. BV2 Membrane-Coated PEGylated-Liposomes Delivered hFGF21 to Cortical and Hippocampal Microglia for Alzheimer's Disease Therapy. *Adv Healthc Mater* **13**, e2400125 (2024).
28. Liu, J., Wang, T., Dong, J. & Lu, Y. The blood-brain barriers: novel nanocarriers for central nervous system diseases. *J Nanobiotechnology* **23**, 146 (2025).
29. Zhang, Q. et al. Meningeal lymphatic drainage: novel insights into central nervous system disease. *Signal Transduct Target Ther* **10**, 142 (2025).
30. Liu, M. et al. Lymph-targeted high-density lipoprotein-mimetic nanovaccine for multi-antigenic personalized cancer immunotherapy. *Sci Adv* **10**, eadk2444 (2024).
31. Zhao, Q. et al. Sleep restoration by optogenetic targeting of GABAergic neurons reprograms microglia and ameliorates pathological phenotypes in an Alzheimer’s disease model. *Molecular Neurodegeneration* (2023).
32. Sasidharan Nair, V., Plazzi, G. & Tucci, V. Neuroimmune interactions in sleep regulation: Epigenetic interfaces between microglia and T cells in brain homeostasis and dysfunction. *Sleep Medicine Reviews* (2026).
33. Hu, Y. et al. Sleep Deprivation Triggers Mitochondrial DNA Release in Microglia to Induce Neural Inflammation: Preventative Effect of Hydroxytyrosol Butyrate. *Antioxidants* (2024).
34. Wei, S.-N. et al. Microglial VDAC1 signaling modulates sleep deprivation-induced transition to chronic postsurgical pain. *Sleep* (2023).
35. Wang, H.C. et al. BV2 Membrane-Coated PEGylated-Liposomes Delivered hFGF21 to Cortical and Hippocampal Microglia for Alzheimer's Disease Therapy. *Advanced Healthcare Materials* (2024).
36. Li, L. et al. Biomimetic Nanoparticles Enhance Recovery of Movement Disorders in Parkinson’s Disease by Improving Microglial Mitochondrial Homeostasis and Suppressing Neuroinflammation. *ACS Applied Materials & Interfaces* (2025).
37. Ding, Y.-N., Li, M.-Q., Ding, P.-T., Wang, P. & Guan, P.-P. Complement C1q-Targeted Microglial Membrane Camouflaged Nanolipid Carriers for Synaptic Protection in Alzheimer’s Disease: A Bioinspired Alectinib Delivery Strategy. *Nano Letters* (2025).
38. Liu, J. et al. Microglial TMEM119 binds to amyloid-β to promote its clearance in an Aβ-depositing mouse model of Alzheimer’s disease. *Immunity* (2025).
39. Flemming, A. Sleep deprivation whips up cytokine storm. *Nature Reviews Immunology* **24**, 1 (2024).
40. Parhizkar, S. et al. Sleep deprivation exacerbates microglial reactivity and Aβ deposition in a TREM2-dependent manner in mice. *Science Translational Medicine* **15** (2023).

41. Li, X., Kong, Z., Cai, K., Qi, F. & Zhu, S. Neopterin mediates sleep deprivation-induced microglial activation resulting in neuronal damage by affecting YY1/HDAC1/TOP1/IL-6 signaling. *Journal of Advanced Research* **72**, 181–195 (2025).
42. Liu, J. et al. Microglial TMEM119 binds to amyloid-β to promote its clearance in an Aβ-depositing mouse model of Alzheimer's disease. *Immunity* **58**, 1830–1846.e1837 (2025).
43. Jung, E.S., Choi, H. & Mook-Jung, I. Decoding microglial immunometabolism: a new frontier in Alzheimer's disease research. *Molecular Neurodegeneration* **20**, 1–29 (2025).
44. Verduzco Espinoza, A.P. et al. Microglia-to-neuron signaling links APOE4 and inflammation to enhanced neuronal lipid metabolism and network activity. *Proceedings of the National Academy of Sciences of the United States of America* **122** (2025).
45. Inoue, Y. et al. Impact of APOE on cerebrovascular lipid profile in Alzheimer's disease. *Acta Neuropathologica* **150** (2025).
46. Zhang, N., Lin, J. & Chew, S.Y. Neural Cell Membrane-Coated Nanoparticles for Targeted and Enhanced Uptake by Central Nervous System Cells. *ACS Appl Mater Interfaces* **13**, 55840–55850 (2021).
47. Liu, H. et al. Targeting Microglia for Therapy of Parkinson's Disease by Using Biomimetic Ultrasmall Nanoparticles. *J Am Chem Soc* **142**, 21730–21742 (2020).
48. Sha, S. et al. Engineered Stem Cell Membrane-Coated Nanodrugs for Targeted Therapy of Alzheimer's Disease. *ACS Appl Mater Interfaces* **17**, 47497–47511 (2025).
49. Dash, P., Das, K. & Dash, M. Mimicking the osteosarcoma surfaceome on nanoparticles for targeted gene therapy. *Biomaterials Science*, 13 (2025).
50. Yin, Y. et al. Targeted Microglial Membrane-Coated MicroRNA Nanosponge Mediates Inhibition of Glioblastoma. *ACS Nano* **18**, 29089–29105 (2024).
51. Antoine et al. Structural and functional features of central nervous system lymphatic vessels. *Nature* (2015).
52. Ahn, J.H. et al. Meningeal lymphatic vessels at the skull base drain cerebrospinal fluid. *Nature* **572** (2019).
53. Dagum, P. et al. The glymphatic system clears amyloid beta and tau from brain to plasma in humans. *Nature Communications* **17** (2026).
54. Zhao, D. et al. Targeting the glymphatic system: Aβ accumulation and phototherapy strategies across different stages of Alzheimer's disease. *Translational Neurodegeneration* **2025** (2025).
55. Parhizkar, S. et al. Sleep deprivation exacerbates microglial reactivity and Aβ deposition in a TREM2 -dependent manner in mice. *Science Translational Medicine* (2023).
56. Sang, D., Lin, K. & Yang, Y., GuangdiLi, BohanChen, ChenLi, QiMa, YanLu, LihuiCui, Xi-YangLiu, ZhiboLv, Sheng-QingLuo, MinminLiu, QinghuaLi, YulongZhang, Eric Erquan Prolonged sleep deprivation induces a cytokine-storm-like syndrome in mammals. *Cell* **186** (2023).

57. Victor, M.B. et al. Lipid accumulation induced by APOE4 impairs microglial surveillance of neuronal-network activity. *Cell Stem Cell* (2022).
58. Wesseling, H. et al. Tau PTM Profiles Identify Patient Heterogeneity and Stages of Alzheimer's Disease. *Cell* (2020).
59. Li, L. et al. Advances in Recombinant Adeno-Associated Virus Vectors for Neurodegenerative Diseases. *Biomedicines* (2023).
60. Sun, J. & Roy, S. Gene-based therapies for neurodegenerative diseases. *Nature Neuroscience* (2021).
61. Sharif, A. et al. The therapeutic potential of probucol and probucol analogues in neurodegenerative diseases. *Translational Neurodegeneration* (2024).
62. Roh, K. et al. Lysosomal control of senescence and inflammation through cholesterol partitioning. *Nature Metabolism* (2023).

Figures

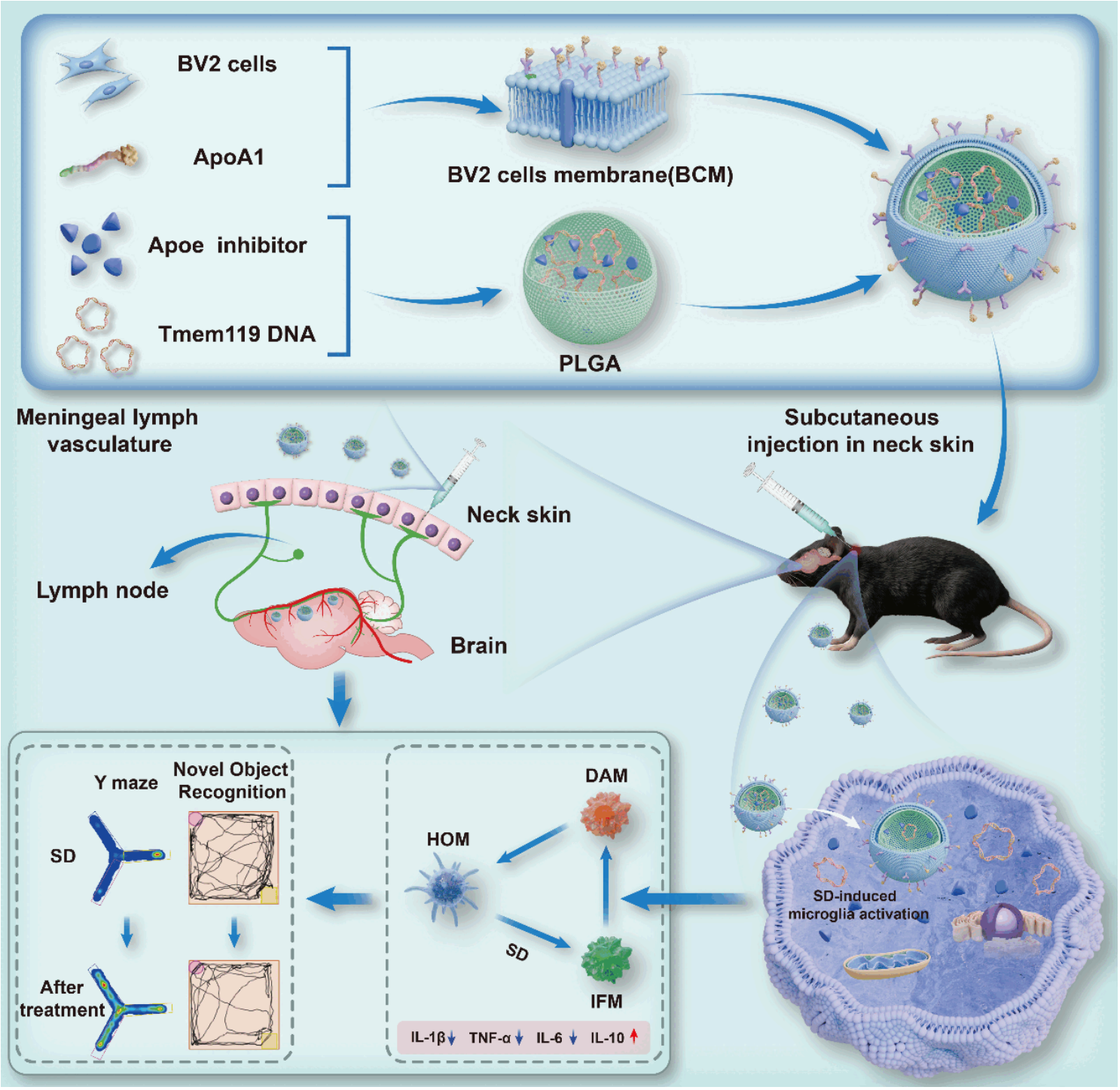


Figure 1

Schematic illustration of the lymphotropic biomimetic nanoplatform (ATABP) for targeted microglial reprogramming and cognitive rescue in sleep deprivation.

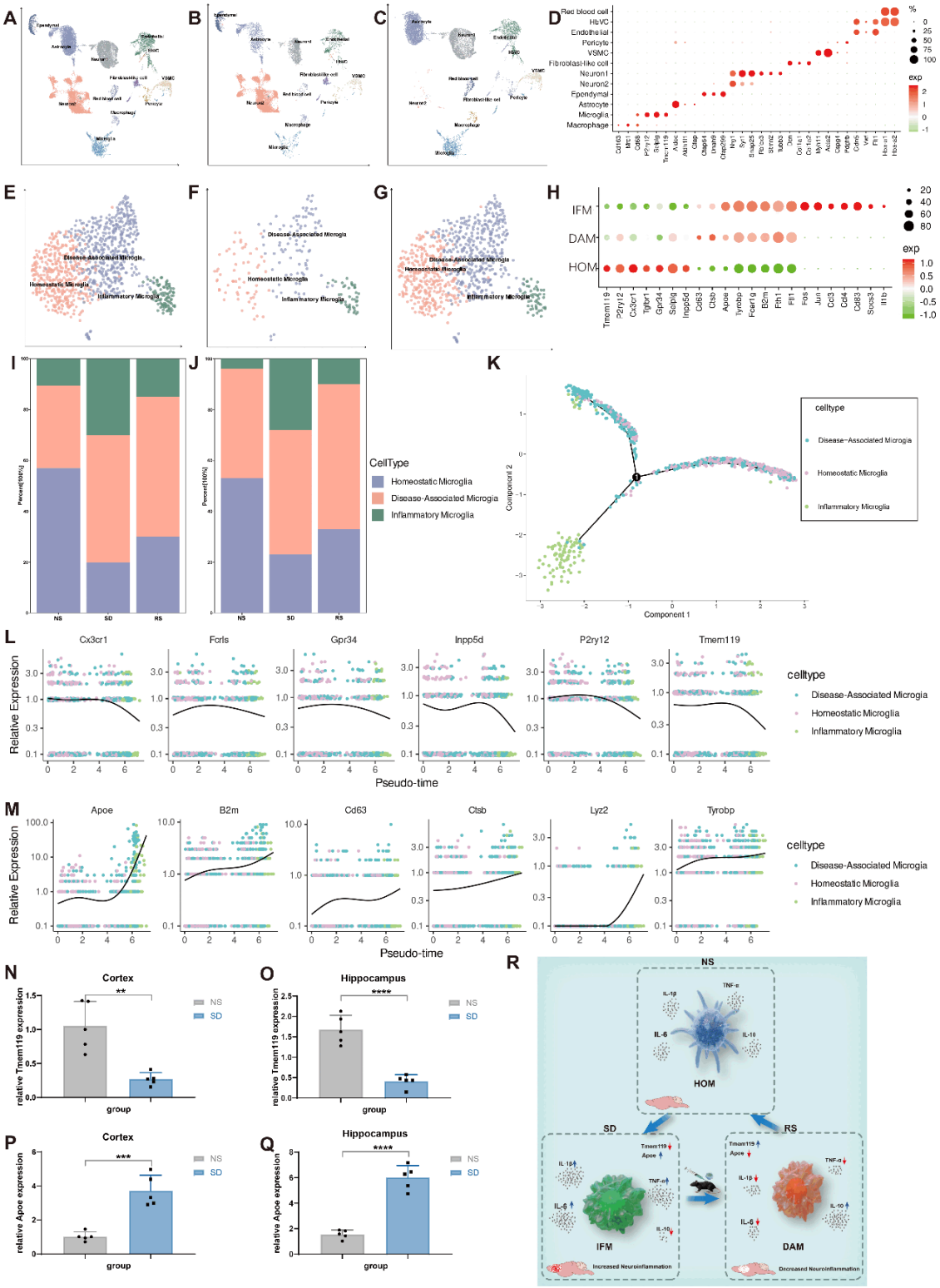


Figure 2

Single-cell transcriptomic analysis identifies an irreversible Tmem119/Apoe imbalance as a driver of sleep deprivation-induced microglial pathology.

A. UMAP visualization of all major cell types from combined cortical and hippocampal tissues across NS, SD, and RS conditions. B-C. UMAP plots of hippocampal (B) and cortical (C) cells colored by cell

type. D. Dot plot showing expression of canonical marker genes used for cell type annotation. E. UMAP of all microglial cells after subclustering, revealing three distinct subpopulations: HOM, DAM, and IFM. F-G. UMAP of microglial subpopulations in hippocampus (F) and cortex (G). H. Dot plot showing expression of subpopulation-specific marker genes. (I-J) Stacked bar graphs quantifying the relative proportions of HOM, DAM, and IFM in hippocampus (I) and cortex (J) across NS, SD, and RS groups. K. Pseudotime trajectory of microglial state transitions. L-M. Expression dynamics of HOM signature genes (L) and DAM signature genes (M) along pseudotime. N-Q. qRT-PCR validation of Tmem119 (N, cortex; O, hippocampus) and Apoe (P, cortex; Q, hippocampus) expression of NS and SD mice (n = 5 per group). (R) Schematic working model illustrating the proposed Tmem119/Apoe imbalance as a therapeutic target for microglial reprogramming. Data are presented as mean ±SEM. *P < 0.05, **P < 0.01, ***P < 0.001, ****P < 0.0001.

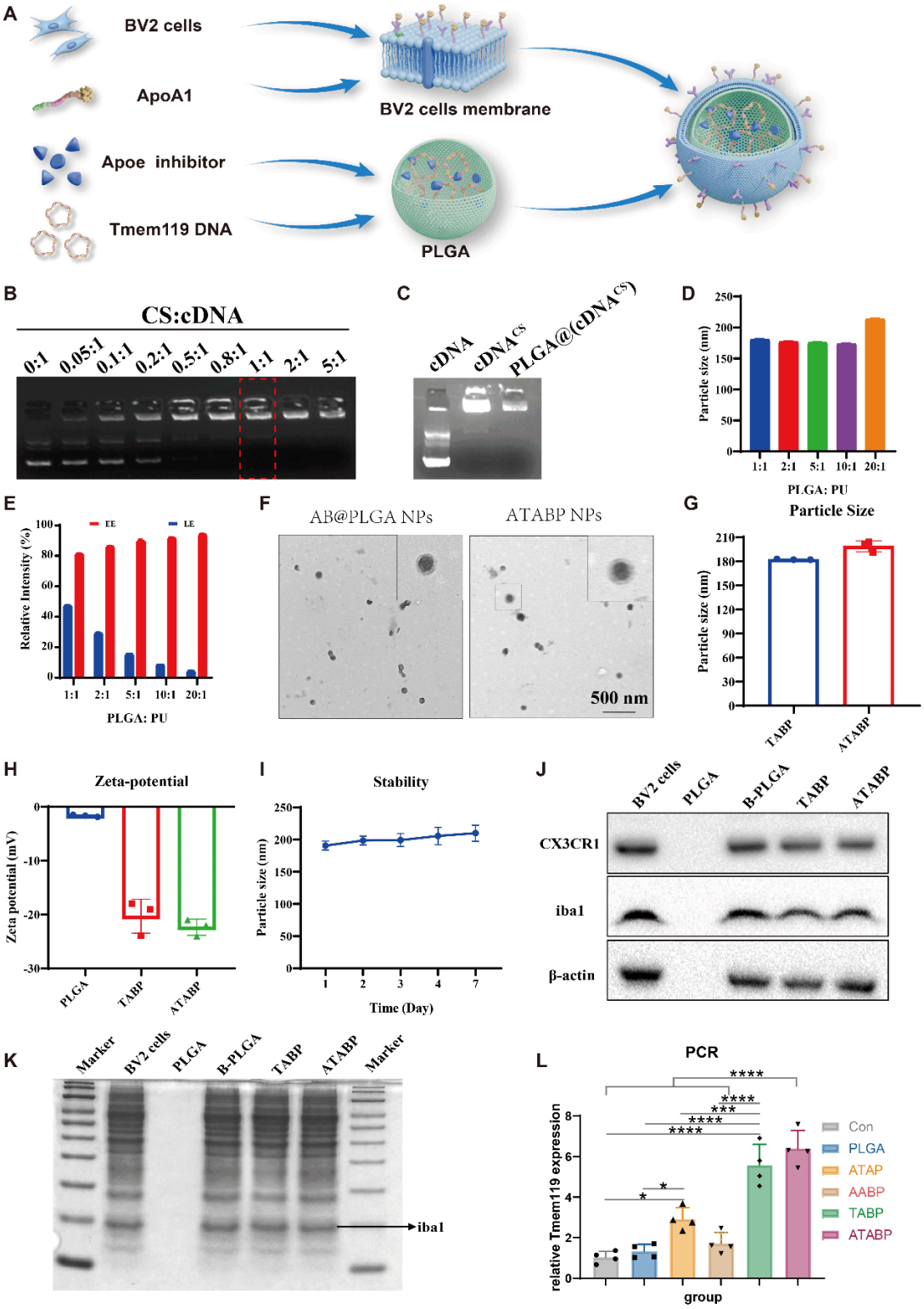


Figure 3

Engineering and characterization of the biomimetic nanoplatform (ATABP).

A. Schematic illustration of the hierarchical ATABP structure. B. Gel retardation assay of CS:cDNA ratios, showing optimal complexation at 1:1 ratio. C. Gel retardation assay confirming successful cDNA encapsulation in CS-cDNA complex and PLGA-loaded complex. D-E. Optimization of PLGA:PU ratio

showing particle size, EE, and LE, with 5:1 selected as optimal. F. TEM images of AB@PLGA, and ATABP. G-H. DLS analysis showing hydrodynamic diameter (G) and zeta potential (H) of ATABP. I. Stability assessment of ATABP in PBS at −20°C over 7 days, showing no significant change in size. J. Western blot confirmation of microglial membrane protein retention (CX3CR1, Iba1) on ATABP compared to membrane lysate. K. Coomassie Blue staining demonstrating preservation of the majority of membrane proteins on ATABP. L. qRT-PCR analysis of Tmem119 expression in BV2 microglia after ATABP treatment, confirming functional gene delivery (n = 4). Data are presented as mean ±SEM. *P < 0.05, **P < 0.01, ***P < 0.001, ****P < 0.0001.

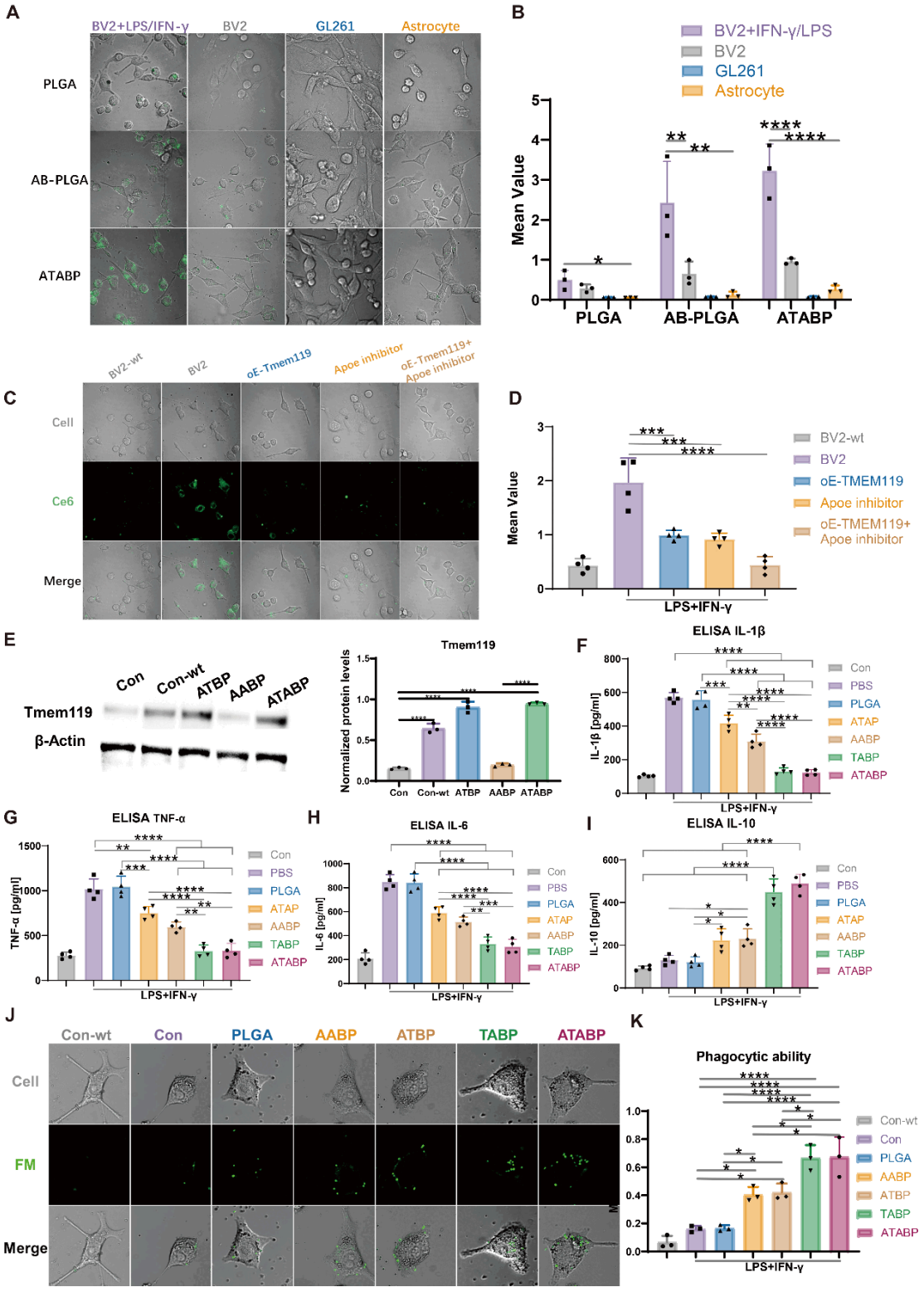


Figure 4

ATABP specifically targets inflammatory microglia and exerts therapeutic reprogramming in vitro.

A-B. Confocal imaging (A) and quantitative analysis (B) of Ce6-labeled nanoparticle uptake by IFN-γ/LPS-activated BV2 microglia, resting BV2 cells, GL261 glioma cells, and primary astrocytes (n = 3). C-D. Confocal imaging (C) and quantitative analysis (D) of ATABP uptake by resting BV2, activated BV2,

activated BV2 overexpressing Tmem119 (Tmem119-OE), activated BV2 treated with APOE inhibitor probucol (PU), and activated BV2 with both Tmem119-OE and PU (n = 4). E. Western blot analysis of Tmem119 protein expression in activated BV2 cells treated with control, AABP, ATBP, or ATABP. F-I. ELISA quantification of pro-inflammatory cytokines IL-1β (F), TNF-α (G), IL-6 (H) and anti-inflammatory cytokine IL-10 (I) in culture supernatants after ATABP treatment (n = 4). J-K. Confocal imaging (J) and quantitative analysis (K) of phagocytic uptake of fluorescent Aβ-mimetic lipid microspheres by activated BV2 cells with or without ATABP treatment (n = 3), FM=Fluorescent micropheres. Data are presented as mean ± SEM. *P < 0.05, **P < 0.01, ***P < 0.001. *P < 0.05, **P < 0.01, ***P < 0.001, ****P < 0.0001.

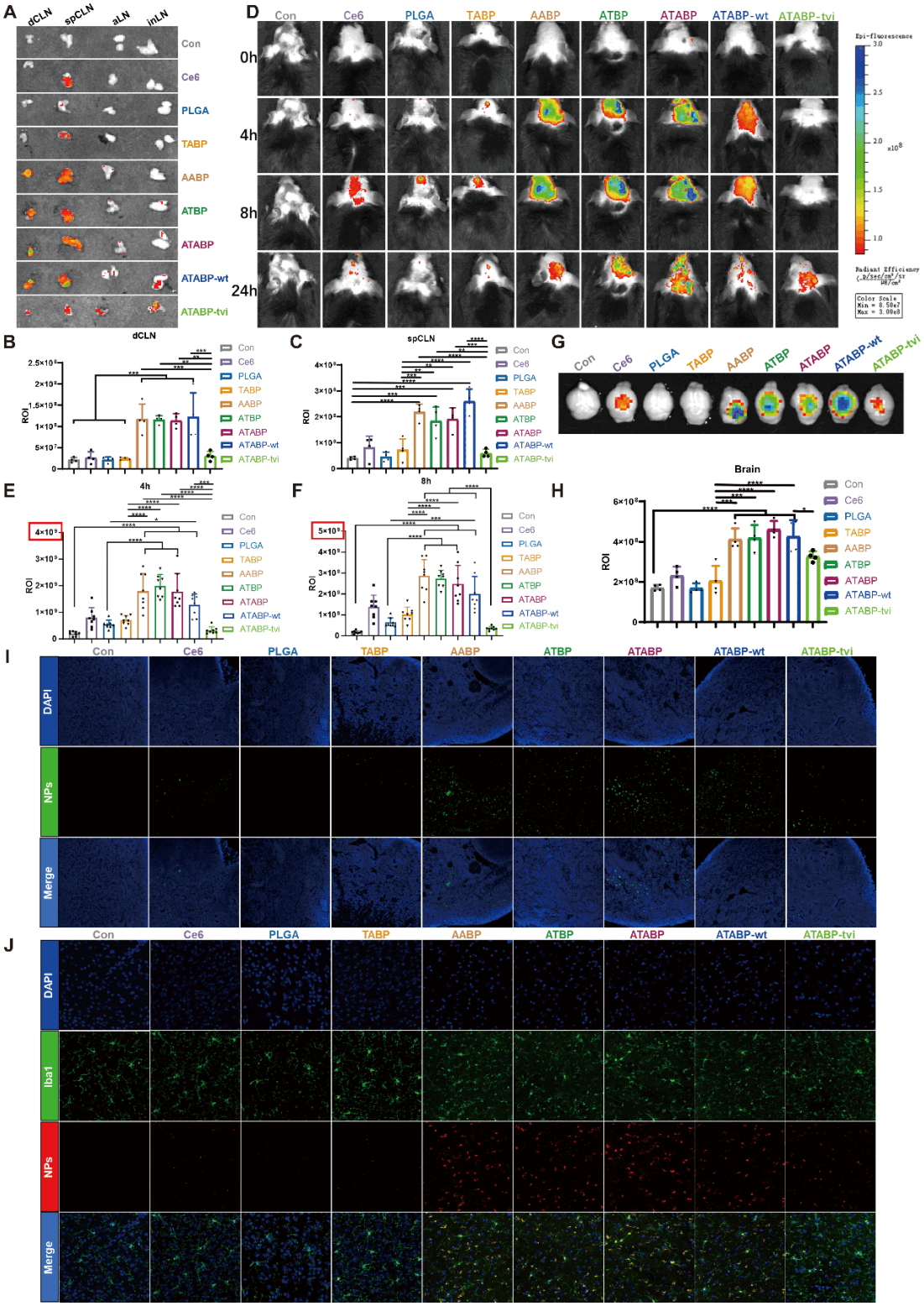


Figure 5

ATABP achieves brain delivery via the lymphatic reverse pathway in vivo.

A-C. Ex vivo fluorescence imaging (A) and quantification of dCLN(B) and spCLN(C) 4 hours after subcutaneous injection of Ce6-labeled PLGA, TABP, AABP, ATBP, or ATABP into mice (n = 4). D-F. Longitudinal in vivo imaging (D) and quantification of brain fluorescence (E-F) over time (0–24 hours)

after subcutaneous injection. G-H. Ex vivo fluorescence imaging (G) and quantification of brain (H) at 8 hours (n = 4). I. Immunofluorescence staining of dCLN showing nanoparticle distribution, NPs= nanoparticles. J. Immunofluorescence co-localization of nanoparticle (red) with Iba1+ microglia (green) in cortical sections. Data are presented as mean ±SEM. *P < 0.05, **P < 0.01, ***P < 0.001. *P < 0.05, **P < 0.01, ***P < 0.001, ****P < 0.0001.

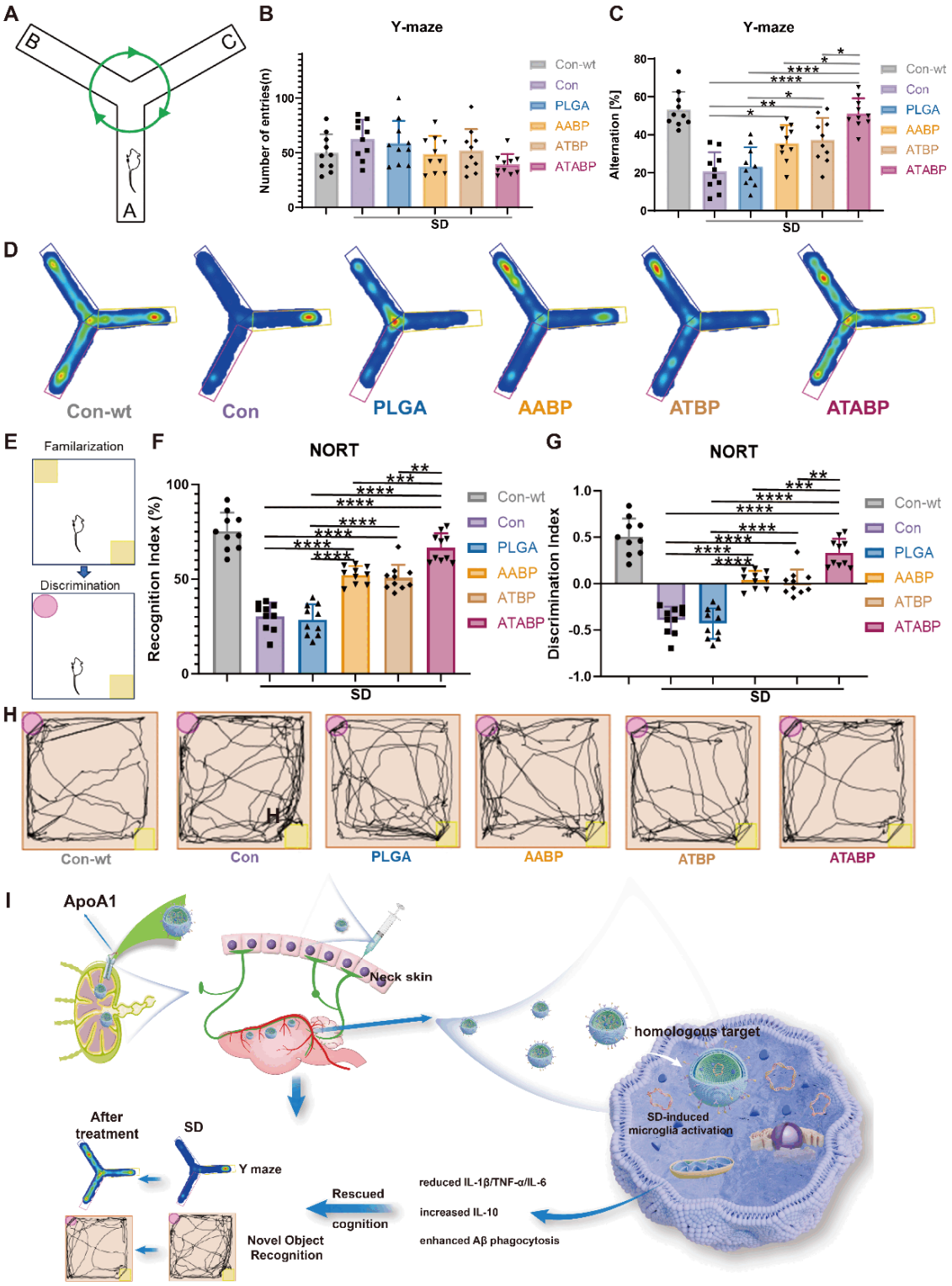


Figure 6

ATABP rescues cognitive deficits in sleep-deprived mice.

A-D. Y-maze test. Schematic of Y-maze apparatus (A), quantification of total arm entries (B), and spontaneous alternation percentage (C) for control, SD, SD+PLGA, SD+AABP, SD+ATBP, and SD+ATABP groups, representative track plots (D) (n = 10). E-H. NOR test. Schematic of NOR paradigm (E), recognition index (F), and discrimination index (G), representative heatmaps (G) (n = 10). (I) Schematic summary of the proposed therapeutic mechanism: subcutaneous injection →cervical lymph node accumulation → meningeal lymphatic trafficking → brain delivery →microglial targeting → Tmem119 restoration and APOE inhibition → cognitive rescue. Data are presented as mean ± SEM. *P < 0.05, **P < 0.01, ***P < 0.001. *P < 0.05, **P < 0.01, ***P < 0.001, ****P < 0.0001.

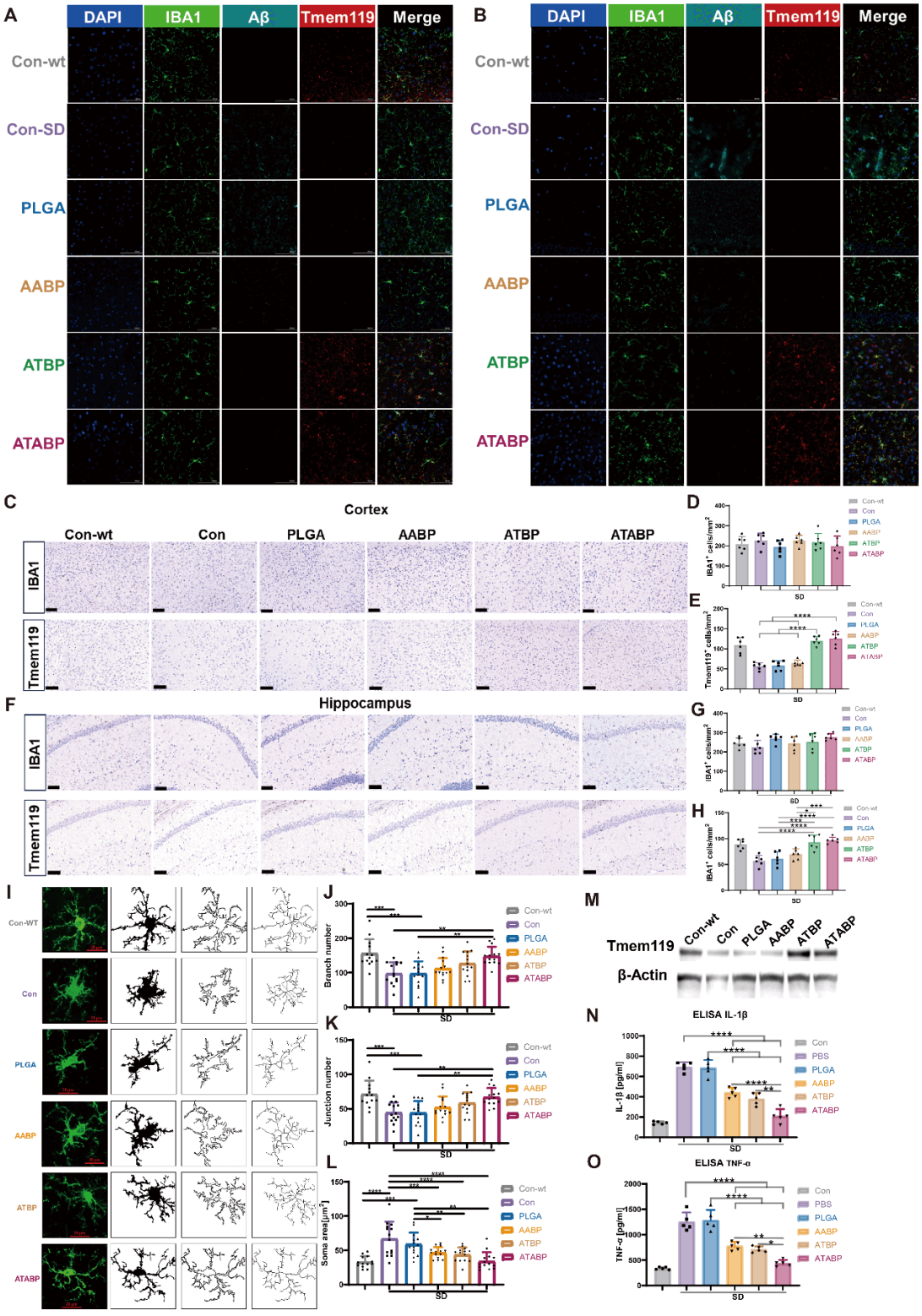


Figure 7

ATABP restores microglial homeostasis, reverses pathological morphology, and suppresses neuroinflammation.

A-B. Representative immunofluorescence images of TMEM119+ microglia and Aβplaque burden in cortex (A) and hippocampus (B) after treatment (n = 4). C-H. Immunohistochemical staining (C, F) and

quantification (D, E, G, H) of Iba1+TMEM119+ double-positive homeostatic microglia in cortex (C-E) and hippocampus (F-H). Scale bars: 50 μm. I-L. Confocal images and Sholl analysis (I) of Iba1-stained microglial morphology, showing branch number (J), junction number (K) and soma area (L) (n = 14-15). Scale bars: 10 μm. M. Western blot analysis of Tmem119 protein expression in brain lysates. N-O. ELISA quantification of IL-1β (N) and TNF-α (O) levels in brain homogenates (n = 5). Data are presented as mean ± SEM. *P < 0.05, **P < 0.01, ***P < 0.001. *P < 0.05, **P < 0.01, ***P < 0.001, ****P < 0.0001.

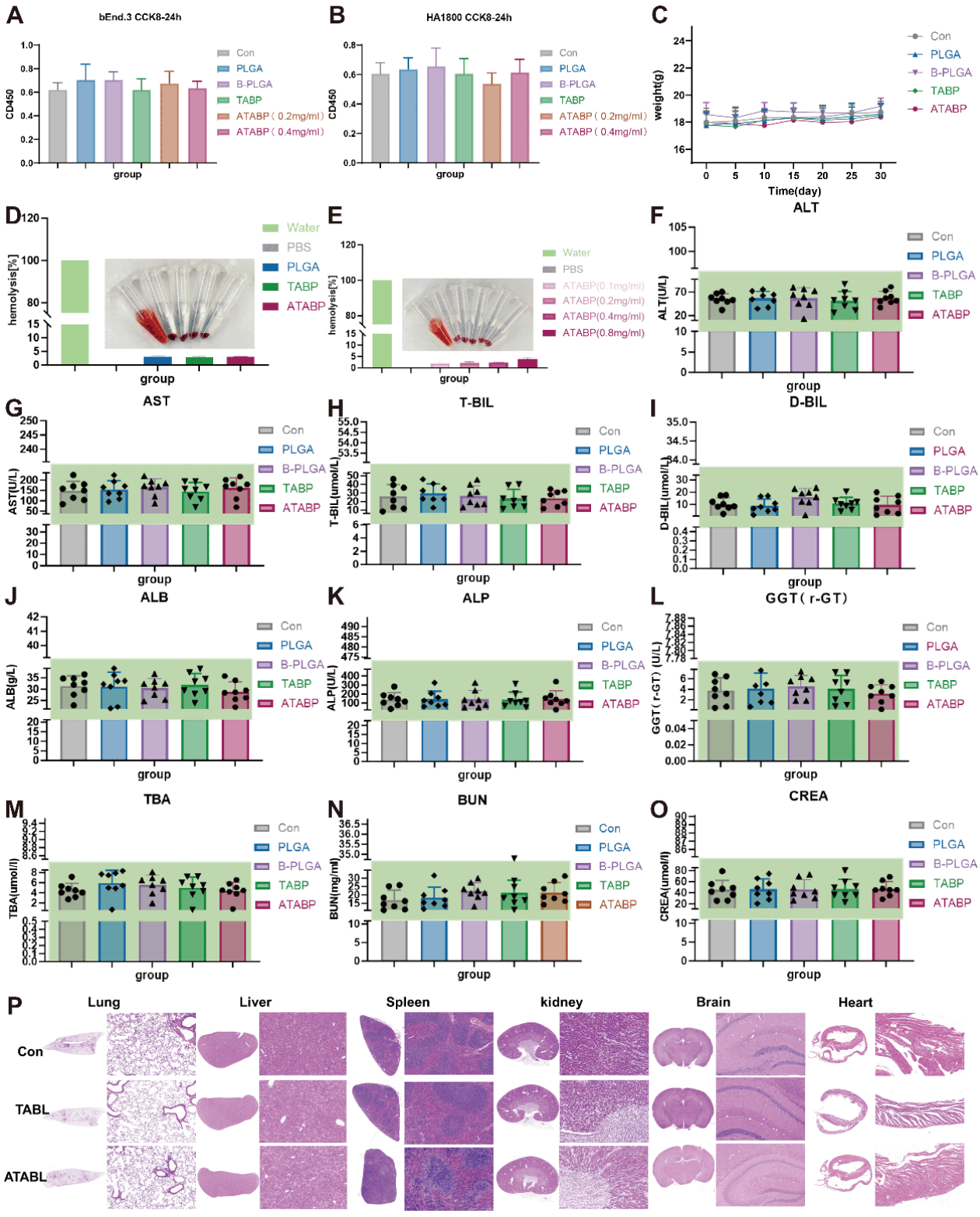


Figure 8

ATABP exhibits a favorable safety profile in vitro and in vivo.

A-B. CCK-8 assay showing cell viability of bEnd.3 brain endothelial cells (A) and HA1800 astrocytes (B) after 24-hour incubation with nanoparticle. (C) Body weight monitoring over 30 days after subcutaneous injection of nanoparticle (n = 6). D-E. Hemolysis assay photographs (D) and quantitative analysis (E) of PLGA, TABP, ATABP (0.1–0.8 mg/mL), with water (100% hemolysis) and PBS (0% hemolysis) as controls (n = 3). F-O.) Serum biochemical analysis of liver function markers—ALT (F), AST (G), T-BIL (H), D-BIL (I), ALB (J), ALP (K), GGT (L), TBA (M)—and kidney function markers—BUN (N), CREA (O)—7 days after injection (n = 8). P. Representative H&E-stained sections of heart, liver, spleen, lungs, kidneys, and brain from PBS-, TABP and ATABP-treated mice 30 days after injection. Data are presented as mean ± SEM.

Supplementary Files

This is a list of supplementary files associated with this preprint. Click to download.

- SupplementaryFigures.docx
- Rawimagefiles.pptx